energies

Article

Influence of Hydraulic Drivetrain Configuration on Kinematic Discrepancy and Energy Consumption during Obstacle Overcoming in a 6 × 6 All-Wheel Hydraulic Drive Vehicle

Mirosław Przybysz [1,*], Marian Janusz Łopatka [1], Arkadiusz Rubiec [1], Piotr Krogul [1], Karol Cieślik [1] and Marcin Małek [2]

[1] Faculty of Mechanical Engineering, Military University of Technology, Kaliskiego 2, 00-908 Warsaw, Poland
[2] Faculty of Civil Engineering and Geodesy, Military University of Technology, Kaliskiego 2, 00-908 Warsaw, Poland
* Correspondence: miroslaw.przybysz@wat.edu.pl; Tel.: +48-261-837-107

Abstract: One of the problems limiting the off-road mobility of multi-axle-wheeled vehicles is a kinematic discrepancy, which increases the resistance to motion when negotiating obstacles. This paper presents the results of research on the possibility of reducing the kinematic discrepancy in vehicles with a hydrostatic drive for each wheel by the appropriate selection of hydraulic components—hydraulic motors and flow dividers. Four different configurations of the drivetrain were tested. They used slow-running hydraulic orbital motors and multi-piston radial motors, as well as gear and spool flow dividers. The tests were conducted with computer simulations based on tests that had already been performed to identify hydraulic parts. They allowed for the assessment of the influence of the characteristics of the components and the configuration of the drive system on the differentiation of the rotational speeds of individual wheels, slippage between the wheels and the ground, and the developed driving torques while overcoming obstacles. These values directly translate into the kinematic discrepancy of the system, the ability to overcome terrain obstacles, and energy consumption.

Keywords: hydrostatic drivetrains; energy consumption; kinematic discrepancy; terrain mobility

check for updates

Citation: Przybysz, M.; Łopatka, M.J.; Rubiec, A.; Krogul, P.; Cieślik, K.; Małek, M. Influence of Hydraulic Drivetrain Configuration on Kinematic Discrepancy and Energy Consumption during Obstacle Overcoming in a 6 × 6 All-Wheel Hydraulic Drive Vehicle. *Energies* **2022**, *15*, 6397. https://doi.org/10.3390/en15176397

Academic Editor: Kim Stelson

Received: 1 August 2022
Accepted: 26 August 2022
Published: 1 September 2022

Publisher's Note: MDPI stays neutral with regard to jurisdictional claims in published maps and institutional affiliations.

1. Introduction

For many years, hydrostatic drives have been used to drive Earth-moving machinery and high-mobility vehicles [1–5]. Due to their resistance to overloads, they are widely used in equipment in which there are large and fast load changes during operation [6,7] or there is a need to smoothly change the driving speed in the entire speed range from 0 to the maximum speed and when it is advisable to drive at speeds that creep [8]. However, it should be noted that hydrostatic drives are characterized by the fairly large influence of the structure of the system and its configuration on the total efficiency of the drive system and the effectiveness of machines and vehicles [9,10]. Particularly noteworthy are mobile machines [11–13], which must efficiently carry out technological activities and independently and efficiently move around the field with the lowest possible energy consumption.

One of the most critical factors determining the capabilities of mobile machines and vehicles for efficient off-road movement is the ability to overcome terrain obstacles. In the case of wheeled vehicles moving on soft terrain with low load capacity and adhesion, to reduce skids and the probability of becoming stuck, efforts are made to ensure the high kinematic stiffness of the drive system; there should not be a significant speed difference between wheels. As a result, axle and inter-axle differential locks are used in the mechanical drive systems of multi-axle vehicles [1,14,15]. For the same purpose, flow dividers are used in hydrostatic drive systems [3,4,6]. On the other hand, the high efficiency of the driveline requires a similar value for the slip of all wheels relative to the ground. As a result, when negotiating obstacles, the wheels should rotate at different rotational speeds depending on the kinematic discrepancy [14,15]. Therefore, it is advisable to shape the kinematic discrepancy of the drive wheels, which undoubtedly causes energy consumption during driving. In the case of the hydrostatic drives of vehicles and multi-axle machines with all-wheel drive, the cooperation of the drive wheels with the ground plays a particularly important role in the context of energy consumption and their instantaneous load, which undoubtedly affects the operating parameters and efficiency of hydraulic components [8,16] and, consequently, the overall efficiency of the drive system and energy consumption.

Eckert et al. [17], in their work, focused on examining the possibility of using multi-domain optimization design and power management control in hydraulic hybrid vehicles in various configurations of the structure of the drive system. As a result of the research, they managed to increase the range of the vehicle, but the study was limited only to driving on a paved road. Sokar and Murrenhoff [18] conducted preliminary simulation studies of the impact of the drive system configuration on the overall efficiency and fuel consumption of the vehicle. The research showed the possibility of a reduction in fuel consumption by approximately 30%, only by changing the operating parameters. However, as in [17], they were limited to the load characteristics of the motor vehicle on firm ground. Azzam et al. [19] demonstrated a beneficial effect on energy consumption of applications in a hybrid hydrostatic drive system instead of the conventional variable displacement pump or multi-piston digital pump. In a sense, this may correspond to driving over large, uneven terrain, which periodically increases and decreases the load.

Papers [17–19] concerned mainly motor vehicles. The developed models focused on the issues of modeling the drive systems themselves and their structures and did not consider the interaction between the wheel and the ground. As a result, they did not take into account the wheel slip and the existing kinematic discrepancy, the resulting changes in driving torques and engine rotational speeds, and changes in their efficiency.

Another issue discussed in the literature is the influence of using control algorithms on the efficiency of hydrostatic drive systems. This problem is equally as important as the properly selected structure of the drive system. Mulders et al. [20] demonstrated the impact of a properly selected algorithm controlling the hydrostatic drive (torque control of the hydraulic motor) on the total efficiency of the drive system. Burgos et al. [21] demonstrated the possibility of using the fuzzy control system to control the engine speed in a hydrostatic transmission. The papers [20,21] were limited only to stationary hydrostatic drives. Attempts to assess the impact of control algorithms in a mobile machine while working in rugged terrain with the simultaneous overcoming of terrain obstacles on the smoothness of movement, taking into account the dynamics of the machine, were made by Zavadinka and Krissak [22]. In their research, Cook et al. [23] attempted to examine the proposed algorithms for controlling the hydrostatic drive system on the mobility of heavy-duty tracked vehicles through traction control based on instantaneous traction force-slip values. A similar problem was investigated by Bodin A. [24] when moving a tracked vehicle in the winter when it has a limited grip and cannot carry much snow.

The problems of active (with the use of control algorithms) traction force control and the rotational speed of the wheels, discussed in [20–24], concern mainly the movement of vehicles on flat ground. An alternative approach to increasing the off-road mobility of all-wheel-drive machines and all-wheel-drive vehicles equipped with hydrostatic drive systems is the use of passive wheel speed control, which does not require complex control algorithms. This requires the introduction of flow dividers into the drive system. However, one should be aware that introducing them into the drive system changes the overall efficiency of the drive system, resulting in energy consumption and the kinematic stiffness of the drive system [8,16,25], which directly translates into the kinematic discrepancy. However, these works largely concern motor vehicles or focus on energy consumption research only for one selected type of flow divider without a significant change in its performance characteristics.

Gear and spool dividers, whose working principles and characteristics differ significantly [16,26,27], are the two most common types of dividers used in machines and vehicles currently. The objective of this study was to determine the effect of altering the configuration of the hydrostatic drive system by combining different types of flow dividers with different types of hydrostatic motors on the energy consumption and kinematic discrepancy of 6 × 6 all-wheel-drive multiple-axle vehicles when encountering obstacles.

2. Materials and Methods

Research on the influence of the hydraulic drivetrain configuration on kinematic discrepancy and energy consumption when overcoming obstacles in a 6 × 6 all-wheel-drive multiple-axle vehicle was conducted in a simulation environment based on a previously developed model [16]. A co-simulation method was used to achieve a good representation of hydraulic drivetrain properties. The developed co-simulation model consisted of two collaborative submodels—the vehicle body model and the hydraulic drivetrain model. The first represented the mechanical structure and properties of the vehicle, and the second represented the hydrostatic drivetrain properties. The combination of hydraulic and mechanical models made it possible to simulate the mutual dynamic interactions and their impact on the efficiency of the drive system. The model was developed on the basis of an existing 6 × 6 skid-steered, hydrostatically driven mobile robot (Figure 1).

(**a**) (**b**)

Figure 1. View of a 3D CAD model of the robot (**a**) and 6 × 6 robot (**b**) [14].

The robot (Figure 1) weight was approximately 4 t. It was equipped with an independent hydropneumatic suspension, a manipulator, and a loader attachment. The robot hydrostatic drivetrain (Figure 2) consisted of variable displacement pumps (1, 2) and hydraulic motors of the left (3, 4, 5) and right side (6, 7, 8) mounted directly inside the wheels. They created two independent hydrostatic transmissions for the left and right sides of the vehicle.

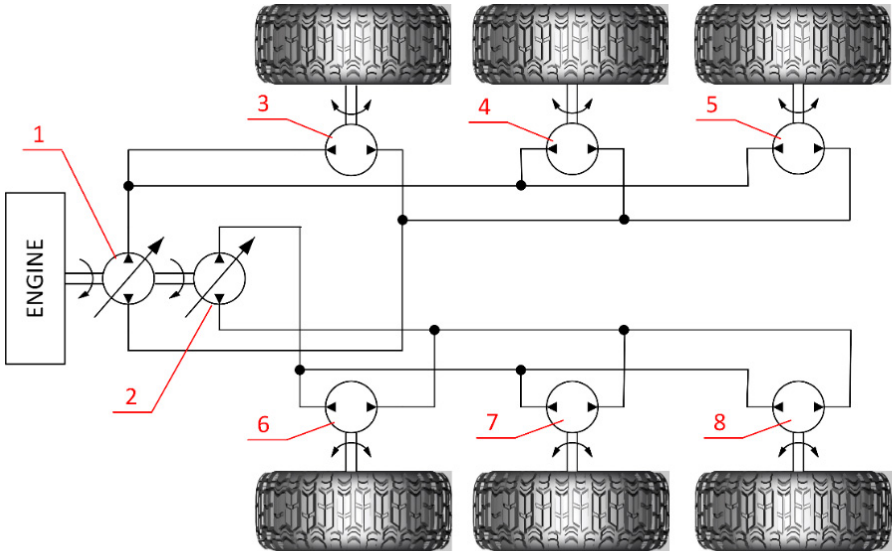

Figure 2. Main elements of the 6 × 6 robot hydrostatic drivetrain: 1, 2—variable displacement pumps; 3, 4, 5—robot left-side hydraulic motors; 6, 7, 8—robot right-side hydraulic motors [14].

2.1. Vehicle Body Model

A half-vehicle body model (Figure 3) was developed. It consisted of three wheels driven by hydrostatic motors. The kinematic structure of the suspension system of the vehicle body model reflected the kinematics of real object suspension (Figure 1). The total mass of the vehicle body model was half the mass of the robot.

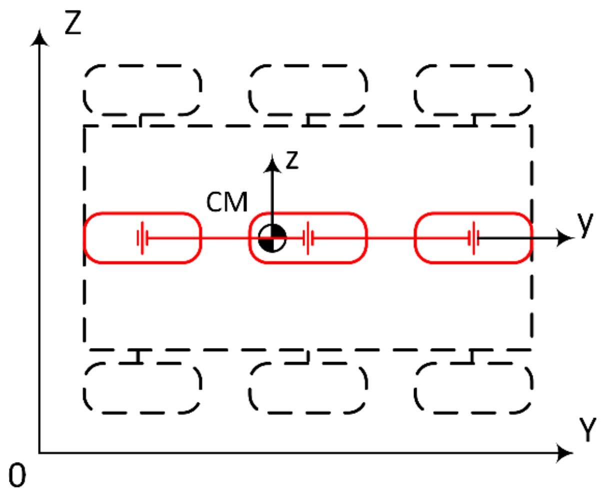

Figure 3. Concept of half-vehicle model [14].

The half-vehicle model was developed with a multi-body method given in Adams 2014.0.1 (MSC Software Corporation). The assumed principle of the vehicle model is shown in Figure 4, and its parameter values are presented in Table 1. The half-vehicle body model had 3 DoF (degrees of freedom): two translational y and x and one rotational φ. Suspension arms were connected (rotational) with the vehicle body at points G, H, and I. Hydropneumatic suspension components were replaced in the model by stiffness/damping elements with linear characteristics. These elements connected the suspension arms with the body between pairs of points: A–D, B–E, and C–F.

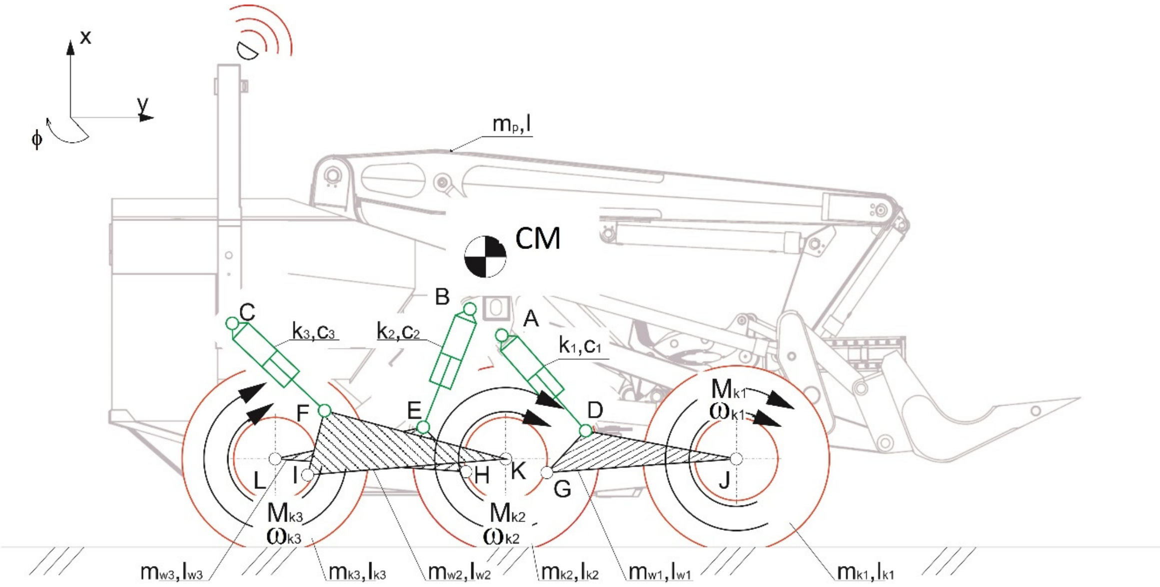

Figure 4. Structure and main parameters of half-vehicle multi-body model [14]: m/I—Mass/mass moment of inertia of vehicle, suspension arms and wheels; M—torque, ω—rotational velocity; k,c—stiffness and damping; A-K—kinematic joints.

Table 1. Values of main vehicle body parameters [16].

Type	Parameter Value
Mass/mass moment of inertia	m_p = 1469.5 kg I = 3234 kgm^2 m_{w1} = 109.8 kg I_{w1} = 10.4 kgm^2 m_{w2} = 112.8 kg I_{w2} = 12.5 kgm^2 m_{w3} = 92.1 kg I_{w3} = 7.9 kgm^2 $m_{k1} = m_{k2} = m_{k3}$ = 39.7 kg $I_{k1} = I_{k2} = I_{k3}$ = 4.08 kgm^2
Stiffness/damping of the spring-damping elements of the suspension	k_1 = 209,000 N/m c_1 = 22,570 Ns/m k_2 = 154,800 N/m c_2 = 16,720 Ns/m k_3 = 674,000 N/m c_3 = 54,600 Ns/m
Wheel radius Wheel base	R = 0.4 m 2 × 1.1 m

The values of masses and mass moments of inertia of particular model parts and the location of the resultant vehicle center of gravity (CM) were obtained based on the 3D CAD (CATIA v5 version release 2016 (Dessault Systems, Dassault Systèmes, Vélizy-Villacoublay, France)) vehicle model and catalog data of the main robot component manufacturers. The holonomic constraints that were used in the vehicle model to connect its parts were ideal (without friction).

The vehicle model used a discrete model of a flexible wheel consisting of rigid bodies forming two circuits: the tire carcass and tire tread. The discrete elements were connected to each other and to the rim by forces and torques derived from stiffness and damping in the radial and circumferential directions; see Figure 5.

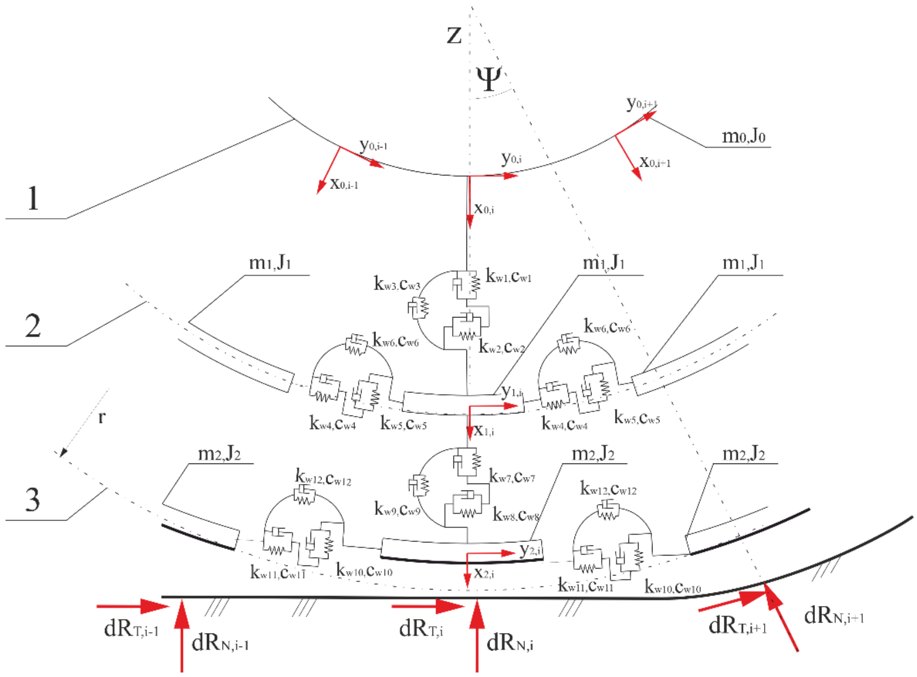

Figure 5. Wheel model structure: 1—wheel rim; 2—carcass; 3—thread; $dR_{N,i}$—elementary normal reaction of the substrate; $dR_{T,i}$—elementary tangential reaction of the substrate; ψ_i—angle of operation of an elementary normal force measured from a vertical line Z [14].

Each rim consisted of 144 elements. Thus, the model met the computational efficiency requirements in accordance with the recommendations contained in [27]. Figure 6 shows the forces acting on the contact between the wheel and the flexible ground, which were taken into account in the developed wheel model.

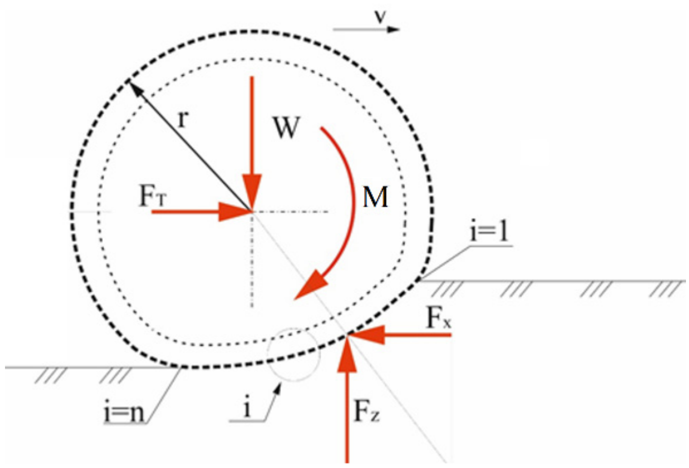

Figure 6. The forces acting on the wheel on soft surface: i—treat element; n—last treat elements in contact with ground number; W—vertical load of wheel; F_T—pulling force [16].

Each element of the wheel tread in contact with the ground surface generates a traction force depending on the slip, the value of the traction coefficient, and the normal reaction to the ground. The main wheel model parameters are presented in Table 2.

Table 2. Values of main wheel model parameters [16].

Wheel Element	Parameter Type	Symbol	Parameter Value
Rim	Mass	m_o	10 kg
	Inertia	J_o	1.120 kgm^2
Carcass	Mass	m_1	0.07 kg
	Inertia	J_1	0.0171 kgm^2
	Number of elements	-	72
	Stiffness	k_{w1}	100,000 N/m
		k_{w2}	100,000 N/m
		k_{w3}	1 Nm/rad
		k_{w4}	10,000,000 N/m
		k_{w5}	20 N/m
		k_{w6}	1 Nm/rad
	Damping	c_{w1}	10,000 Ns/m
		c_{w2}	500 Ns/m
		c_{w3}	500 Nms/rad
		c_{w4}	100 Ns/m
		c_{w5}	100 Ns/m
		c_{w6}	1 Nms/rad
Tread	Mass	m_2	0.07 kg
	Inertia	J_2	0.0224 kgm^2
	Number of elements	-	72
	Stiffness	k_{w7}	500,000 N/m
		k_{w8}	500,000 N/m
		k_{w9}	1 Nm/rad
		k_{w10}	5,000,000 N/m
		k_{w11}	5,000,000 N/m
		k_{w12}	1 Nm/rad
	Damping	c_{w7}	500 Ns/m
		c_{w8}	500 Ns/m
		c_{w9}	0.1 Nms/rad
		c_{w10}	100 Ns/m
		c_{w11}	100 Ns/m
		c_{w12}	0.1 Nms/rad

The vertical load on the wheel is balanced by the sum of the vertical components of the elementary forces—normal and tangential—acting at the contact point of the tire with the ground (Figure 6), which, in the developed model, was determined based on the dependence

$$W = F_z = \sum_{i=1}^{n} (dR_{N,i} \cos\psi + dR_{T,i} \sin\psi) \tag{1}$$

where $dR_{N,i}$ is the elementary normal reaction of the ground; $dR_{T,i}$ is the elementary tangential reaction of the ground [15].

In agreement with the abovementioned dependence, the pulling force results from the difference in the horizontal components of normal and tangential forces acting in contact with the ground, according to

$$F_T = F_X = \sum_{i=1}^{n} (dR_{T,i} \cos\psi - dR_{N,i} \sin\psi) \tag{2}$$

The driving force was determined according to

$$F_D = F_Z \varphi \tag{3}$$

where φ is the traction coefficient. Hence, the driving torque is expressed as

$$M_N = F_D \cdot r_d \tag{4}$$

where r_d is the wheel dynamic radius.

The developed model allowed us to obtain different traction coefficient values depending on slip; see Figure 7. The dependency of the traction coefficient on the slip value of the wheel model is similar to the characteristics found in the literature [15,17,28–30]. The slip factor is defined as the ratio between the theoretical wheel velocity (resulting from its angular velocity and dynamic radius) and the actual velocity.

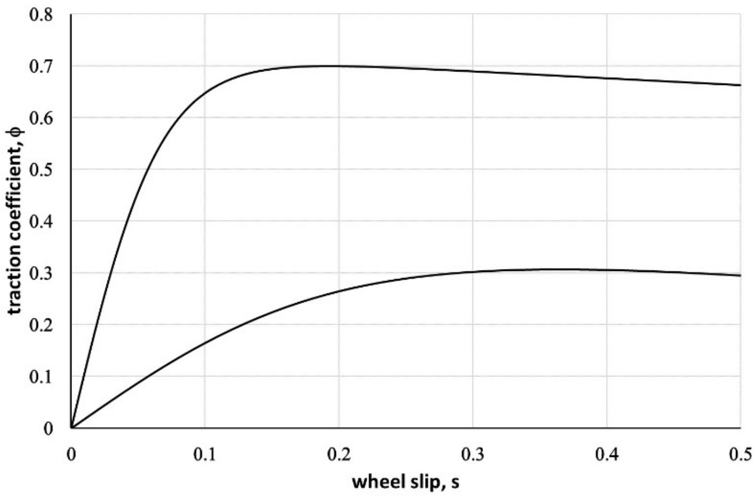

Figure 7. Plot of the traction coefficient of the wheel model as a function of slip.

2.2. Hydraulic Drivetrain Model

The hydraulic drivetrain model (Figure 8) for the half-vehicle body model was developed in a separate software program (Easy5 2015.0.1 Version 9.1.1 (MSC Software Corporation, Newport Beach, CA, USA)). To examine the influence of the hydraulic drivetrain configuration on the energy consumption and kinematic discrepancy of a 6 × 6 all-wheel-drive multiple-axle vehicle during the overcoming of obstacles, the system structure shown in the figure was assumed (Figure 2). Different types of hydrostatic motors and flow dividers were considered. A hydraulic flow divider is a unit that should theoretically share the flow between the hydraulic motors. The values that connect the vehicle body model and the hydraulic drivetrain model are as follows: drive torques on the wheels M_{ki} and their angular velocities ω_{ki}.

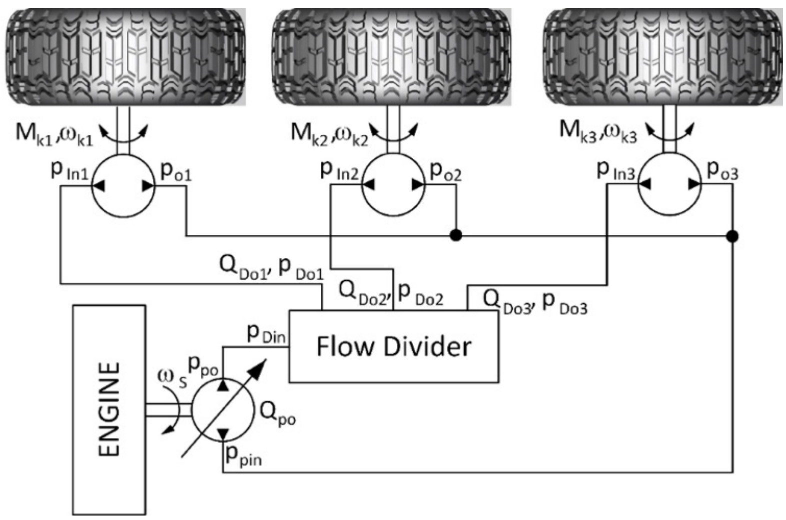

Figure 8. Concept of a hydrostatic drivetrain model for half-vehicle body model [14].

The driving torque M_{ki} generated by the i-th wheel in the model of the hydraulic drive system caused increases in the value of the pressure drop Δp_i on the hydraulic motor of this wheel:

$$\Delta p_i = p_{Ini} - p_{oi} \tag{5}$$

where p_{Ini} is the pressure on the input of the hydraulic motor; p_{oi} is the pressure on the output of the hydraulic motor.

The pressure on the hydraulic motor input depends on the pressure drop Δp_i and on the driving torque value M_{ki}:

$$p_{Ini} = \frac{M_{ki}}{q_s \cdot \frac{\eta_{os}}{\eta_{vs}}} + p_{oi} \tag{6}$$

where q_s is the hydraulic motor displacement; η_{os} is the overall efficiency of the hydraulic motor; η_{vs} is the volumetric efficiency of the hydraulic motor. The overall and volumetric efficiency of hydraulic motors depends on the motor type and the values of pressure and angular velocity, η_{os}, $\eta_{vs} = f(\Delta p_i, \omega_{ki})$, which change during vehicle driving.

The pressure p_{Doi} on the i-th output of the flow divider is greater than the value p_{Ini} shown by the pressure drop value Δp_i resulting from flow resistance occurring on the pipes Δp_{Li} and hydraulic connections Δp_{mi}, which are mounted between the divider and the motor:

$$\Delta p_i = \Delta p_{Li} + \Delta p_{mi} \tag{7}$$

The pressure drop in the hydraulic pipes Δp_{Li} mainly depends on the value of the friction factor f, length L_i of the i-th pipe/hose, its hydraulic diameter D_{hLi}, and flow velocity V_{Li}:

$$\Delta p_i = f \frac{L_i}{D_{hLi}} \frac{V_{Li}^2 \rho}{2} \tag{8}$$

where ϱ is the hydraulic oil density.

The flow velocity in the pipe/hose V_i depends on the value of the flow rate Q_{Doi} and hydraulic diameter D_{hLi}:

$$V_{Li} = \frac{4Q_{Doi}}{\pi D_{hLi}^2} \tag{9}$$

The value of the friction factor f depends on the flow character, classified on the basis of the Reynolds number:

$$Re_{Li} = \frac{\rho V_{Li} D_{hLi}}{\mu} \tag{10}$$

where μ is the hydraulic oil dynamic viscosity.

For the laminar flow ($Re_{Li} < 2000$), the friction factor is calculated according to

$$f = \frac{64}{Re_{Li}} \tag{11}$$

In the case of the transition state ($2000 \leq Re_{Li} < 4000$), the friction factor is calculated according to

$$f = \frac{f_{4K} - f_{2K}}{2000} Re_{Li} + 2f_{2K} - f_{4K} \tag{12}$$

where f_{2K} is the value of the friction factor calculated according to (11) for a Reynolds number of 2000; f_{4K} is the value of the friction factor calculated according to (13) for a Reynolds number of 4000.

For turbulent flow ($4000 \leq Re_{Li} \leq Re_{Li\delta}$), the friction factor is calculated according to

$$\frac{1}{\sqrt{f}} = -2\log_{10}\left(\frac{\delta}{3.7} + \frac{2,51}{Re_{Li}\sqrt{f}}\right) \tag{13}$$

where δ is the relative roughness, whereby

$$Re_{Li\delta} = \frac{5000}{\delta} \tag{14}$$

For turbulent flow ($Re_{Li} > Re_{Li\delta}$), the friction factor has a constant value that depends only on the value of $Re_{Li\delta}$, calculated according to (13) for $Re_{Li} = Re_{Li\delta}$.

The pressure drop occurs at the connection elements of hydraulic lines Δp_{mi}, which also depends on the flow character. The laminar flow is calculated according to

$$\Delta p_{mi} = \frac{Q_{Doi} \cdot 2\mu \cdot Re_T}{\pi \cdot D_h^3 \cdot C_d^2} \tag{15}$$

where D_h is the hydraulic diameter of the connection element; C_d is the discharge coefficient; Re_T is the Reynolds number for turbulent flow.

For turbulent flow, the pressure drop is calculated according to

$$\Delta p_{mi} = \frac{8\rho Q_{Doi}}{C_d^2 \cdot \pi^2 \cdot D_h^4} \tag{16}$$

Usually, to calculate the pressure drop for the connection elements, it is assumed that the transition to turbulent flow occurs at a Reynolds number of 100 ($Re_T = 100$). Therefore, there is almost always a turbulent flow.

The pressure drop between input, p_{Din}, and the individual output of the flow divider, p_{Doi}, is also calculated from (16). The pressure value p_{po} at the pump output is higher than the pressure value p_{Din} calculated by the value of the pressure drop resulting from losses (7). The pressure drop Δp_p on the pump is as follows:

$$\Delta p_p = p_{po} - p_{pin} \tag{17}$$

where p_{pin} is the pump input pressure, which is usually 2 MPa for closed circuit systems.

The flow rate Q_{po} generated by the pump depends mainly on its displacement q_p and the angular velocity of the shaft of the engine/pump ω_s:

$$Q_{po} = \frac{60 q_p \omega_s}{2\pi} \eta_{vp} \tag{18}$$

where η_{vp} is the volumetric efficiency of the pump; $\eta_{vp} = f(\Delta p_p, \omega_s)$.

The angular velocity ω_{ki} for the i-th wheel depends on the hydraulic motor displacement q_s and the flow rate Q_{Doi}:

$$\omega_{ki} = \frac{2\pi Q_{Doi}}{60 q_s} \eta_{vs} \tag{19}$$

According to the scope of the research, two hydrostatic drivetrain models were developed:

- One with a gear-type flow divider—Figure 9;
- One with a spool-type flow divider—Figure 10.

In addition to the two types of flow dividers, the tested variants took into account the characteristics corresponding to two types of hydraulic motors: a radial piston motor and an orbital motor. The main hydrostatic drivetrain model parameters are presented in Table 3.

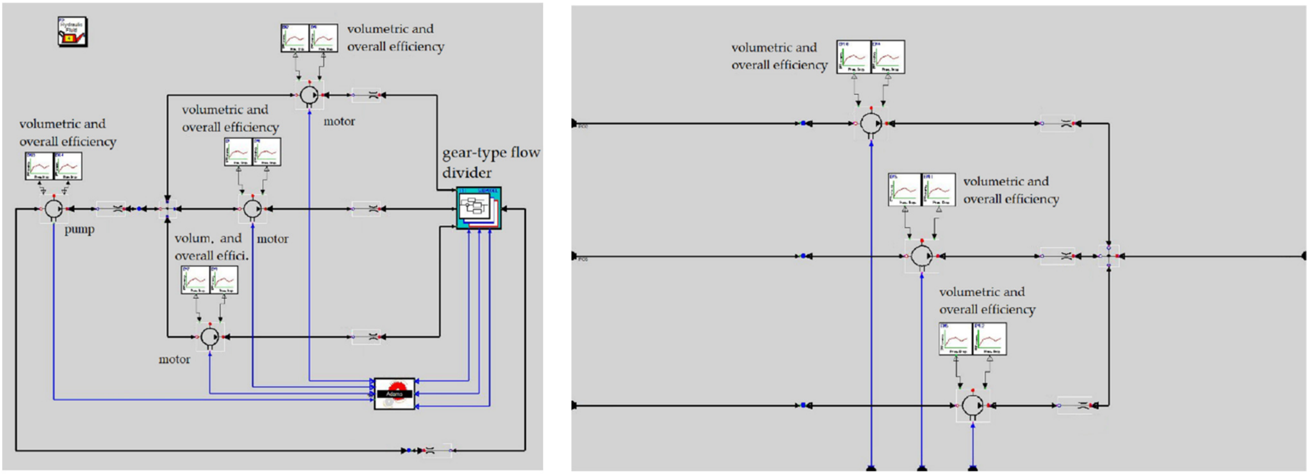

(**a**) (**b**)

Figure 9. Model of the hydrostatic drivetrain with a gear-type flow divider (**a**) and the model of the gear divider (**b**).

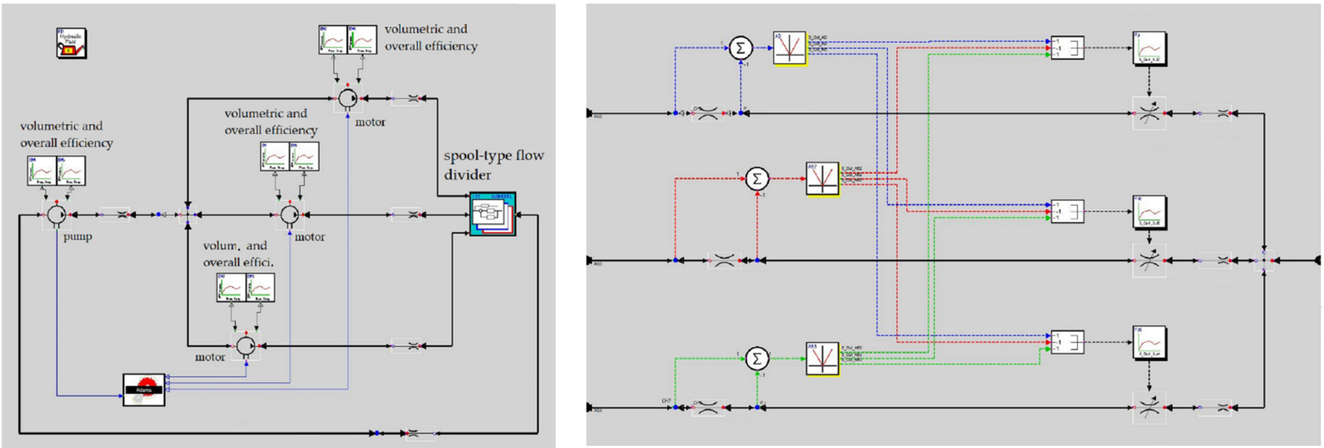

(**a**) (**b**)

Figure 10. Model of the hydrostatic drivetrain with a spool-type flow divider (**a**) and the model of the spool divider (**b**).

Table 3. Values of main hydrostatic drivetrain model parameters.

Parameter	Value
Hydraulic motor displacement (both radial piston and orbital types)	q_s = 500 cm^3/rev
Axial piston pump maximum displacement	q_s = 56 cm^3/rev
Nominal pump flow	100 dm^3/min
Flow divider's nominal flow	80 dm^3/min

In the models (Figures 9 and 10), characteristics were implemented that had been identified during previously conducted laboratory research [27]. The volumetric and overall efficiency and the flow divider's dividing accuracy were identified as a function of a pressure and shaft speed map (Figure 11).

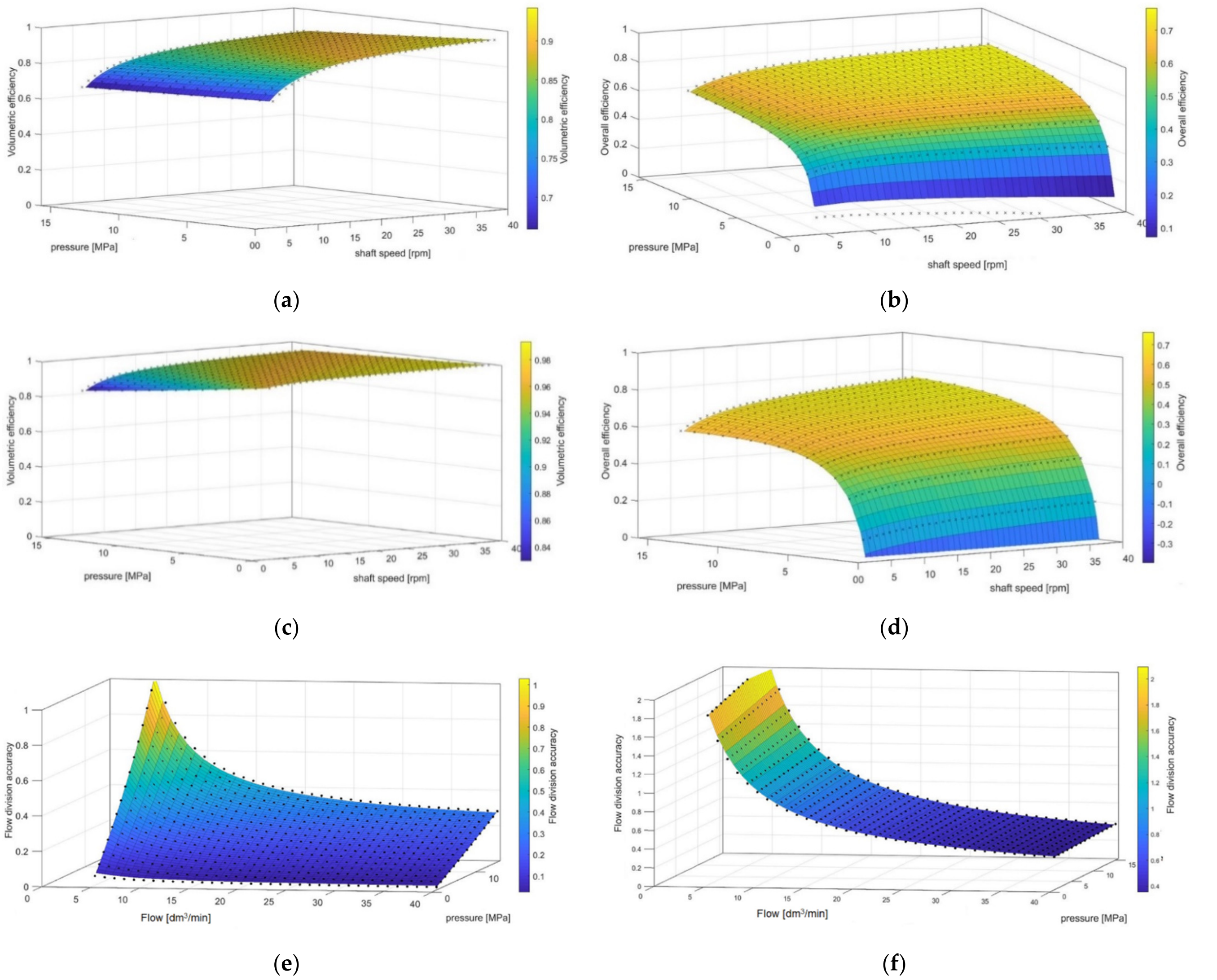

Figure 11. Characteristics of the hydraulic orbital motor volumetric (**a**) and overall (**b**) efficiency, radial piston motor volumetric (**c**) and overall (**d**) efficiency, and spool (**e**) and gear-type (**f**) flow divider's dividing accuracy [17].

2.3. Simulation Setup and Evaluation Indicators

Research on the energy consumption and kinematic discrepancy of a 6 × 6 all-wheel-drive multiple-axle vehicle during the overcoming of obstacles was performed with the following driveline configurations:

1. In a drivetrain with a gear-type flow divider (GD) in combination with
   a. Orbital motors (OM);
   b. Radial piston motors (RM);
2. In a drivetrain with a spool-type flow divider (SD) in combination with
   a. Orbital motors (OM);
   b. Radial piston motors (RM).

In all configurations, vehicle models were driven through obstacles in the form of an earth ditch (Figure 12) that was 2.4 m in length and with two different heights of 0.6 m. In the research, the unevenness of the ground was introduced in the shape of a sinusoid. Earlier preliminary studies [25,26] carried out for a model of a vehicle with a perfectly rigid, kinematically stiff drive system moving on terrain with obstacles of various geometry (ditch, earth embankment, hill) showed that the ditch was the obstacle in the case of which there was the greatest kinematic discrepancy. To compare the actions of the drive system and assess the impact of the tested drive system configurations in various conditions, simulations were conducted for two values of maximum traction coefficient between the wheel and ground, ϕ_{max} 0.3 and 0.7. According to Figure 7, the temporary traction coefficient depends on the wheel slip values.

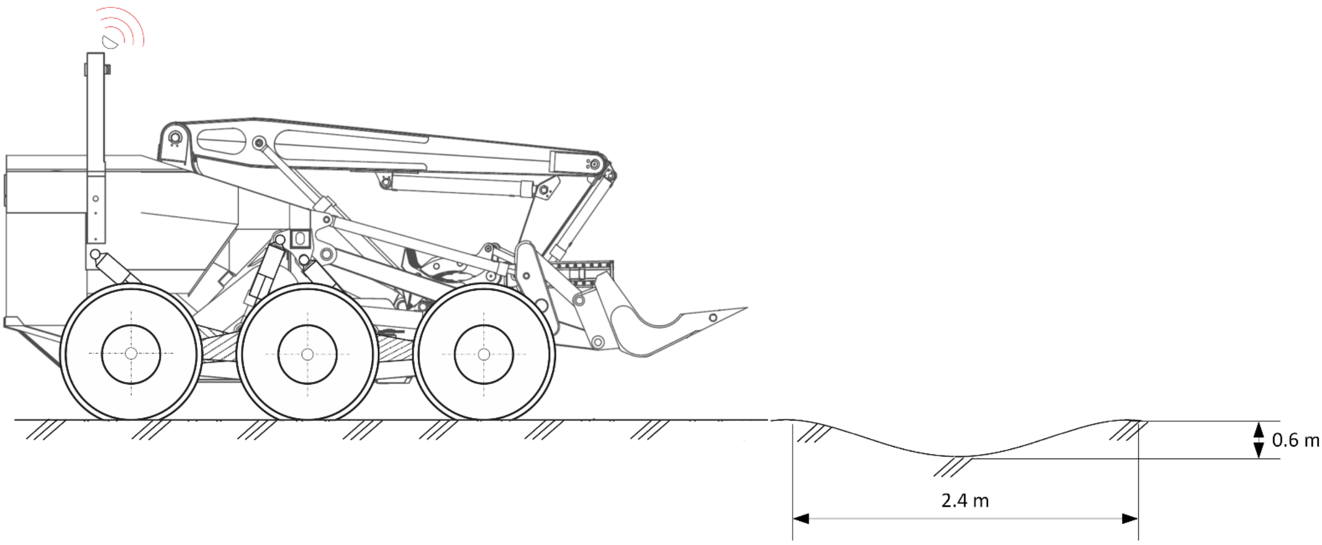

Figure 12. Overall scheme of simulated situation.

In order to reduce the influence of dynamic loads, a theoretical, relatively low speed of 0.8 m/s (3 km/h) was assumed in the model. It was set by the rotational speed of the pump shaft (Figures 9 and 10) and the pump setting. The actual driving rate was lower due to leaks in the hydraulic system (volumetric efficiency of components depends on pressure and rotational speed) and slippage between the wheels and the ground.

The following values were assessed:

- the maximum value of the differences in the rotational speed of the wheels, Δn_{max},

$$\Delta n_{max} = \max_{0 \leq t \leq end} [\Delta n(t)]$$

where n_1 *(t)*, n_2*(t)*, n_3*(t)*—rotational speeds of the wheels,

$$\Delta n(t) = \max_{0 \leq t \leq end} [n_1(t), n_2(t), n_3(t)] - \min_{0 \leq t \leq end} [n_1(t), n_2(t), n_3(t)]$$

- the average value of the differences in the rotational speed of the wheels, Δn_{avg},

$$\Delta n_{avg} = \underset{0 \leq t \leq end}{average} [\Delta n(t)]$$

- the maximum value of wheel slip, s_{max},

$$s_{max} = \max_{0 \leq t \leq end} [s_{max}(t)]$$

where $s_{1,2,3}$*(t)*—wheel slip, $r_{d1,2,3}$ *(t)*—dynamic radius of the wheels, $\omega_{k1,2,3}$—angular velocity of the wheel, $v_{j1,2,3}$—linear speed of the wheel center,

$$s_{max}(t) = \max_{0 \leq t \leq end} [s_1(t), s_2(t), s_3(t)]$$

$$s_1(t) = \left(\frac{\omega_{k1}(t) \cdot r_{d1}(t)}{v_{j1}(t)}\right)^{tanh(v_{j1}(t))}$$

$$s_2(t) = \left(\frac{\omega_{k2}(t) \cdot r_{d2}(t)}{v_{j2}(t)}\right)^{\tanh(v_{j2}(t))}$$

$$s_3(t) = \left(\frac{\omega_{k3}(t) \cdot r_{d3}(t)}{v_{j3}(t)}\right)^{tanh(v_{j3}(t))}$$

- the average value of wheel slip, s_{avg},

$$s_{avg} = \underset{0 \le t \le end}{avarage} \left[s_{max}(t)\right]$$

- the maximum value of the driving torques on the wheels, T,

$$T_{max} = \max_{0 \le t \le end} [T_{max}(t)]$$

where $T_{1,2,3}(t)$—value of driving torques of road wheels,

$$T_{max}(t) = \max_{0 \le t \le end} [|T_1(t)|, |T_2(t)|, |T_3(t)|]$$

- the maximum value of the differences between the driving torques of the wheels, ΔT_{max},

$$\delta T = \max_{0 \le t \le end} [\delta T(t)]$$

where $T_1(t)$, $T_2(t)$, $T_3(t)$—driving torque of road wheels,

$$\delta T(t) = \max_{0 \le t \le end} [|T_1(t)|, |T_2(t)|, |T_3(t)|] - \min_{0 \le t \le end} [|T_1(t)|, |T_2(t)|, |T_3(t)|]$$

- the average value of the driving torques of the wheels, ΔT_{avg},

$$T_{avg}(t) = \frac{|T_1(t)| + |T_2(t)| + |T_3(t)|}{3}$$

$$T_{avg} = \underset{0 \le t \le end}{avarage} \left[T_{avg}(t)\right]$$

The value of the kinematic discrepancy is directly related to the value of the rotational speed of each wheel. At the same time, the energy consumption is related to the rotational speed, slip, and drive torque.

3. Results and Discussion

The performed simulations showed significant differences between the tested configurations.

Figure 13 shows the time histories of the changes in the values of the relative differences in the rotational speeds of road wheels during the simulation when the vehicle model was driven through the ditch with the tested drive system configurations and the values of the adhesion coefficients.

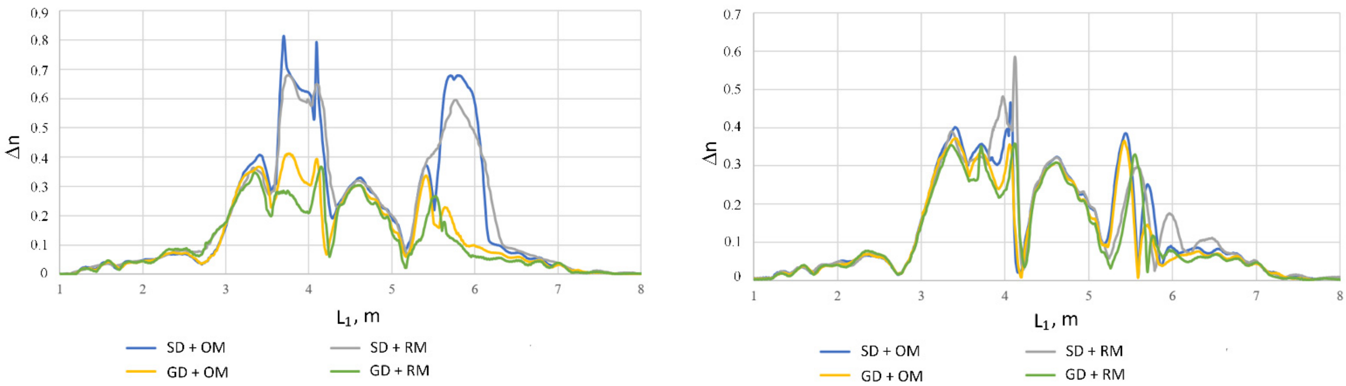

(**a**) (**b**)

Figure 13. The values of the relative differences in the rotational speed of the road wheels during the simulation when the vehicle model was driven through the ditch at the maximum value of the coefficient of adhesion φ = 0.3 (**a**) oraz φ =0.7 (**b**): GD—gear-type flow divider, SD—spool-type flow divider, OM—orbital motor, RM—radial piston motor.

The change in the characteristics of the flow divider (GD or SD) had a much greater impact on the differences in the speed of the road wheels during the simulation than that of the hydraulic motor (OM or RM). It was especially visible when negotiating an obstacle with low adhesion of the substrate (Figure 13a). In the considered case—driving on the ground with the coefficient of adhesion φ = 0.3 with different divisors—the maximum differences between the rotational speed of the wheels and the average speed were as high as Δn_{max} = 0.8.

The value of Δn_{max} for systems with the same flow divider for the different engine types differed by a maximum of 10%. However, in the case of changing the flow divider with the same type of hydraulic motor, they were in the range of 30 ÷ 50%. When overcoming the same obstacle, but with the coefficient of adhesion φ = 0.7 (Figure 13b), such significant differences in rotational speed between the wheels of individual axles were not observed.

A list of the maximum values of the relative difference in rotational speed when driving on the ground with a high or low coefficient of adhesion is presented in Figure 14a, while the values of the average relative speed difference are presented in Figure 14b.

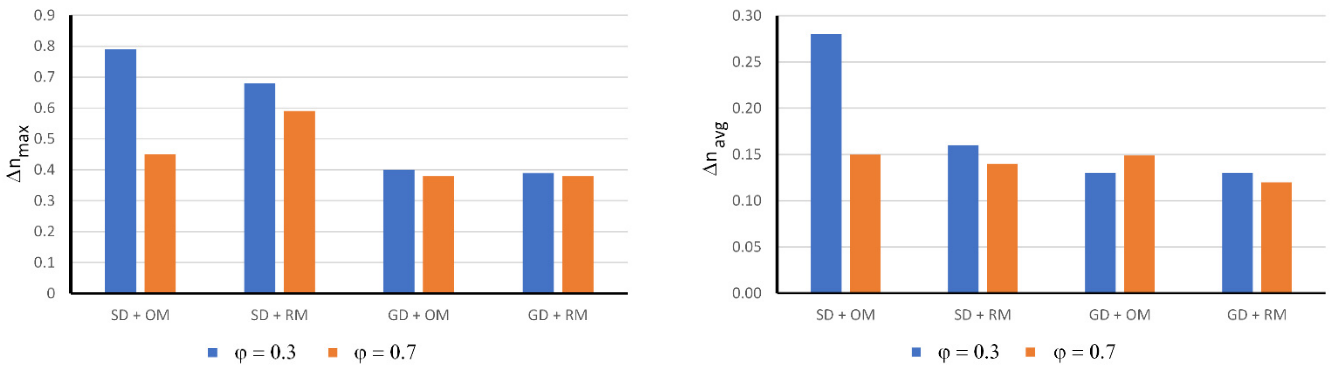

(**a**) (**b**)

Figure 14. List of maximum values (**a**) and average (**b**) relative differences in the rotational speed of the road wheels during the simulation when the vehicle model was driven through the ditch at different maximum values of the adhesion coefficient: GD—gear-type flow divider, SD—spool-type flow divider, OM—orbital motor, RM—radial piston motor.

The maximum differences in rotational speed (Figure 14a) differed in value for different configurations of the driveline and values of the adhesion coefficient. The largest of them occurred in the case of a system in which a slider divider (SD) and a hydraulic orbital motor (OM) were used, and they were then 80%. A much smaller effect of adhesion was observed in the case of systems equipped with a gear flow divider (GD). In this case, regardless of the characteristics of the hydraulic motor, the values were similar and amounted to approximately 40%. Comparing the average values of the difference in rotational speed (Figure 14b), a smaller variation was observed for different components of the drive system. A clear influence of the value of the adhesion coefficient occurred in the configuration SD + OM (slide divider and hydraulic orbital motors). The highest average values also occurred in this configuration. This was due to the lowest kinematic stiffness of the drive system.

The characteristics of the flow divider had a much greater influence on the values of slip (Figure 15), as in the case of the rotational speed than the choice of a hydrostatic motor. This was especially visible when driving on the ground with a lower value of the coefficient of adhesion, equal to $\varphi = 0.3$. The most significant values of wheel slip occurred while driving into the ditch, which initially relieved the front wheel and then the rear wheel. The second moment of increased wheel slipping occurred during the exit from the ditch and resulted from the need to generate greater driving forces.

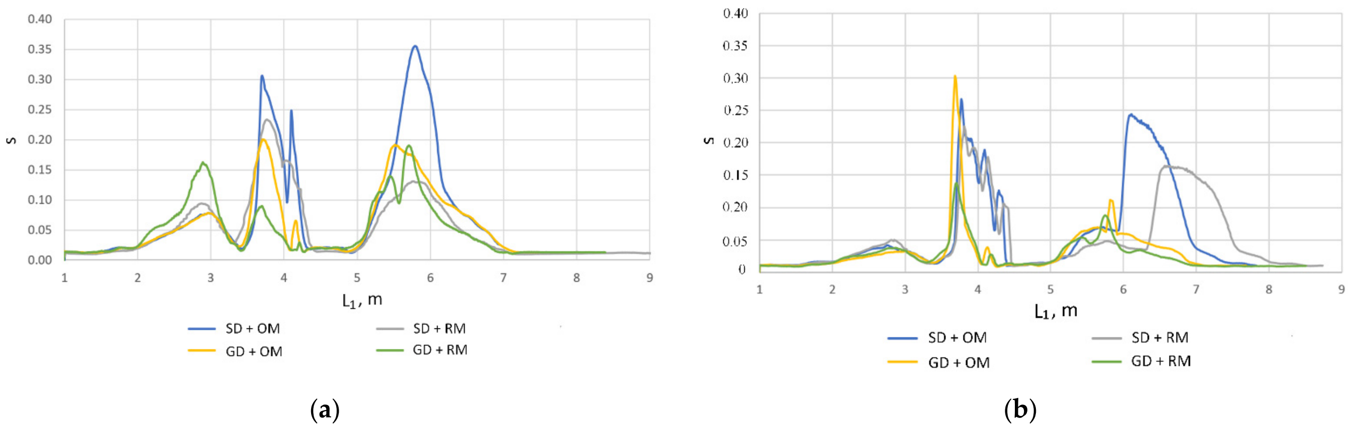

Figure 15. The maximum value from the course of road wheel skidding during the simulation when the vehicle model was driven through the ditch at the maximum value of the coefficient of adhesion $\varphi = 0.3$ (**a**) and $\varphi = 0.7$ (**b**): GD—gear-type flow divider, SD—spool-type flow divider, OM—orbital motor, RM—radial piston motor.

The maximum value in the case of a system equipped with slide dividers (SD), assuming the coefficient of adhesion $\varphi = 0.3$ and $\varphi = 0.7$ was in the range $s = 0.3 \div 0.35$, while, in the case of systems equipped with gear dividers (GD), the slip value was $s = 0.15 \div 0.20$. In the case of a system in which a gear divider (GD) and an orbital motor (OM) were used, the slip values of the wheels were similar to those of the spool divider (SD). This was due to significant leaks in the orbital motor (similar to the level of the slide divider).

A summary of the maximum values (Figure 16) of the sum of wheel slip when driving on the ground with a high or low coefficient of adhesion is shown in Figure 16a, while the values of average wheel slip are shown in Figure 16b.

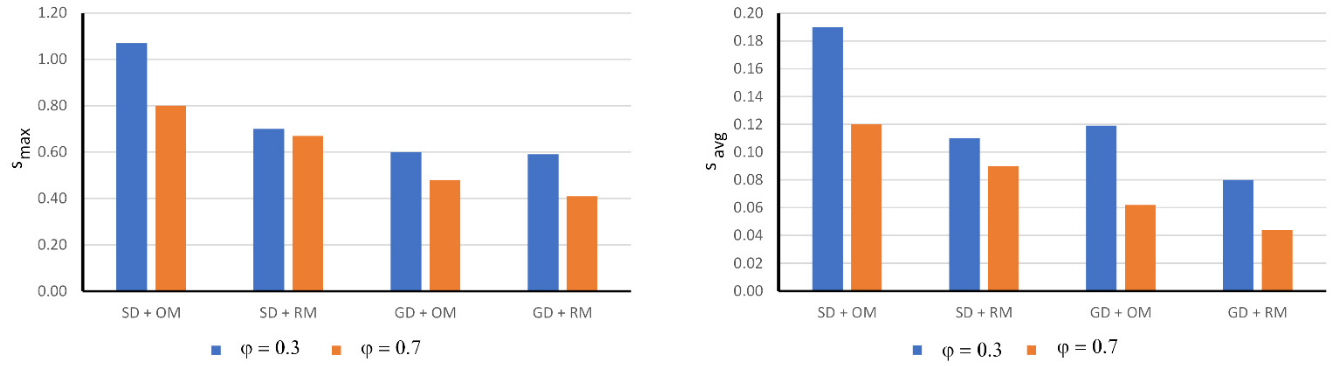

(**a**) (**b**)

Figure 16. Summary of the maximum values (**a**) and average values (**b**) of road wheel skidding during the simulation when the vehicle model was driven through the ditch at different maximum values of the adhesion coefficient: GD—gear-type flow divider, SD—spool-type flow divider, OM—orbital motor, RM—radial piston motor.

In the case of a substrate with a higher coefficient of adhesion s_{max} (Figure 16a), the maximum value occurred for a system consisting of a gear divider (GD) and a hydraulic orbital motor (OM). It amounted to s_{max} = 0.8. In the case of the substrate with a lower value of the adhesion coefficient, the maximum values of s_{max} also occurred for the same configuration and amounted to s_{max} = 1.08. The smallest maximum values of s_{max} were obtained for gear dividers in configuration with radial motors (for both tested values of the coefficient of adhesion). In the case of the substrate with higher adhesion, they amounted to s_{max} = 0.6, and in the case of higher adhesion, s_{max} = 0.4.

The system consisting of a sliding divider (SD) and a hydraulic orbital motor (OM) obtained the highest average values (Figure 16b) for the sum of road wheel slips. This value was s_{max} = 0.19 for the substrate with lower adhesion and s_{max} = 0.12 for higher adhesion. In the case of the other tested configurations, the slip values obtained were within the range s_{max} = 0.04 ÷ 0.12. The lowest value was obtained in the case of a system with a gear divider (GD) and a radial motor (RM).

The tests did not show a significant influence of the kinematic discrepancy compensation on the sum of the values of driving moments occurring on the road wheels (Figure 17). In the cases of both coefficient of adhesion φ = 0.3 and φ = 0, the maximum value of the sum of the driving torques reached values in the range T_{Σ} = 1500 ÷ 2000 Nm.

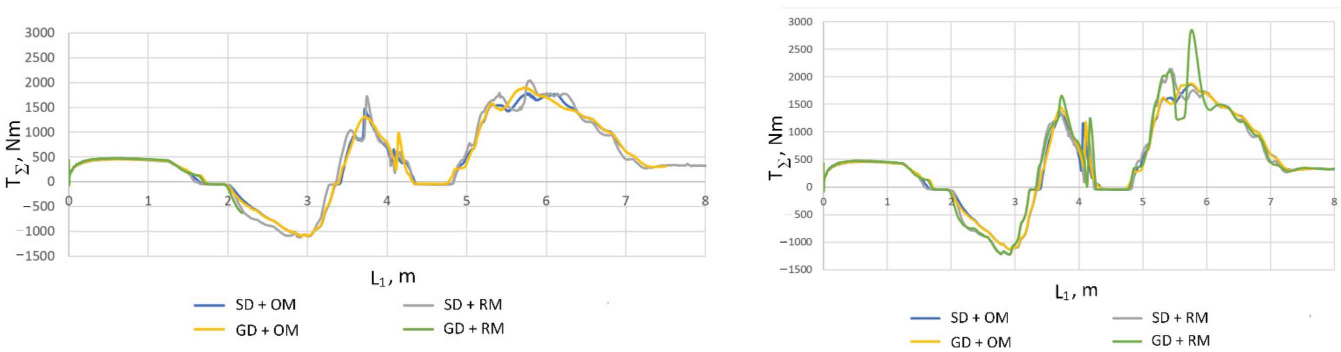

(**a**) (**b**)

Figure 17. Changes in the value of the sum of driving torques on the road wheels during the simulation when the vehicle model was driven through the ditch at the maximum value of the coefficient of adhesion φ = 0.3 (**a**) and φ = 0.7 (**b**): GD—gear-type flow divider, SD—spool-type flow divider, OM—orbital motor, RM—radial piston motor.

On the other hand, the ability to compensate for the kinematic discrepancy had a significant impact on the differences in the driving torque on individual road wheels (Figure 18). The research showed that in the case of using the slide divider for the passage on the ground with a high coefficient of adhesion φ = 0.7, regardless of the type of hydrostatic motor, it was possible to freely adjust the rotational speed of the road wheels to the demand resulting from the shape of the terrain obstacle. This divider was working in the dead zone at this time. When driving on the ground with a lower grip value φ = 0.3, an increase in the load difference was visible due to the operation of the slide flow divider at the moment of unloading one of the road wheels. The fact that the slide divider operated in the non-sensitivity zone while negotiating an obstacle had a positive effect on the loads in the driving system, as it did not cause additional internal elastic tension. Only after exceeding the speed difference limit corresponding to the insensitivity zone caused by the increase in wheel slip was the short-term operation of the divider observed.

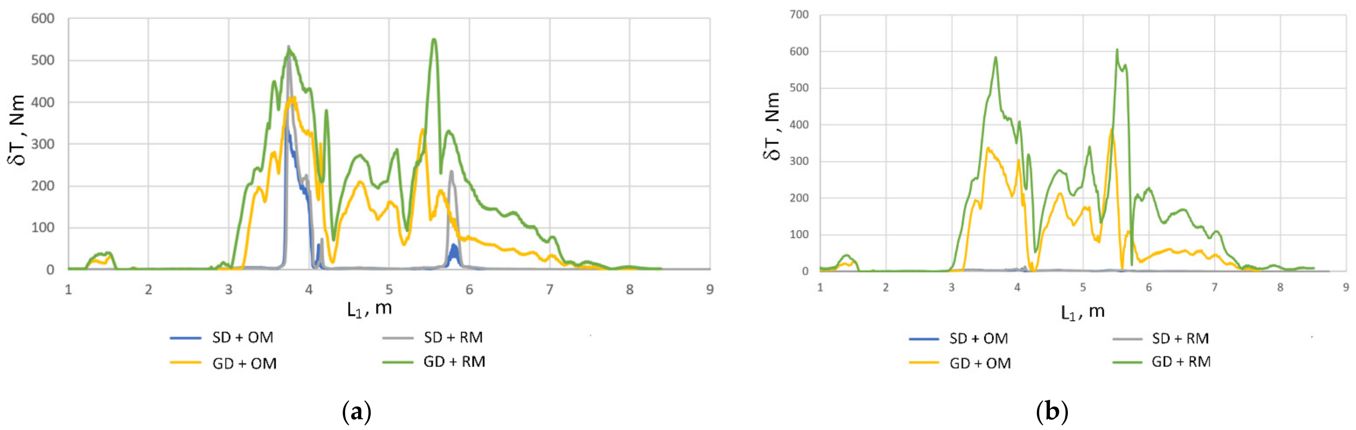

Figure 18. Changes in the difference in driving torques on the road wheels during the simulation when the vehicle model was driven through the ditch at the maximum value of the coefficient of adhesion φ = 0.3 (**a**) oraz φ = 0.7 (**b**): GD—gear-type flow divider, SD—spool-type flow divider, OM—orbital motor, RM—radial piston motor.

The maximum values of the differences in moments in the tested configurations were similar (Figure 19a). The greatest differences occurred in the case of the use of the gear divider and the radial motor. Comparing the values of the maximum torques (Figure 19b), it was observed that the highest value of the driving torques was obtained when using radial motors, both in combination with a gear divider and a slide divider. The smallest average values of the driving torque (Figure 19c) were obtained both in the case of a system consisting of a slide divider and a radial motor (both in the case of a lower and higher value of the coefficient of adhesion).

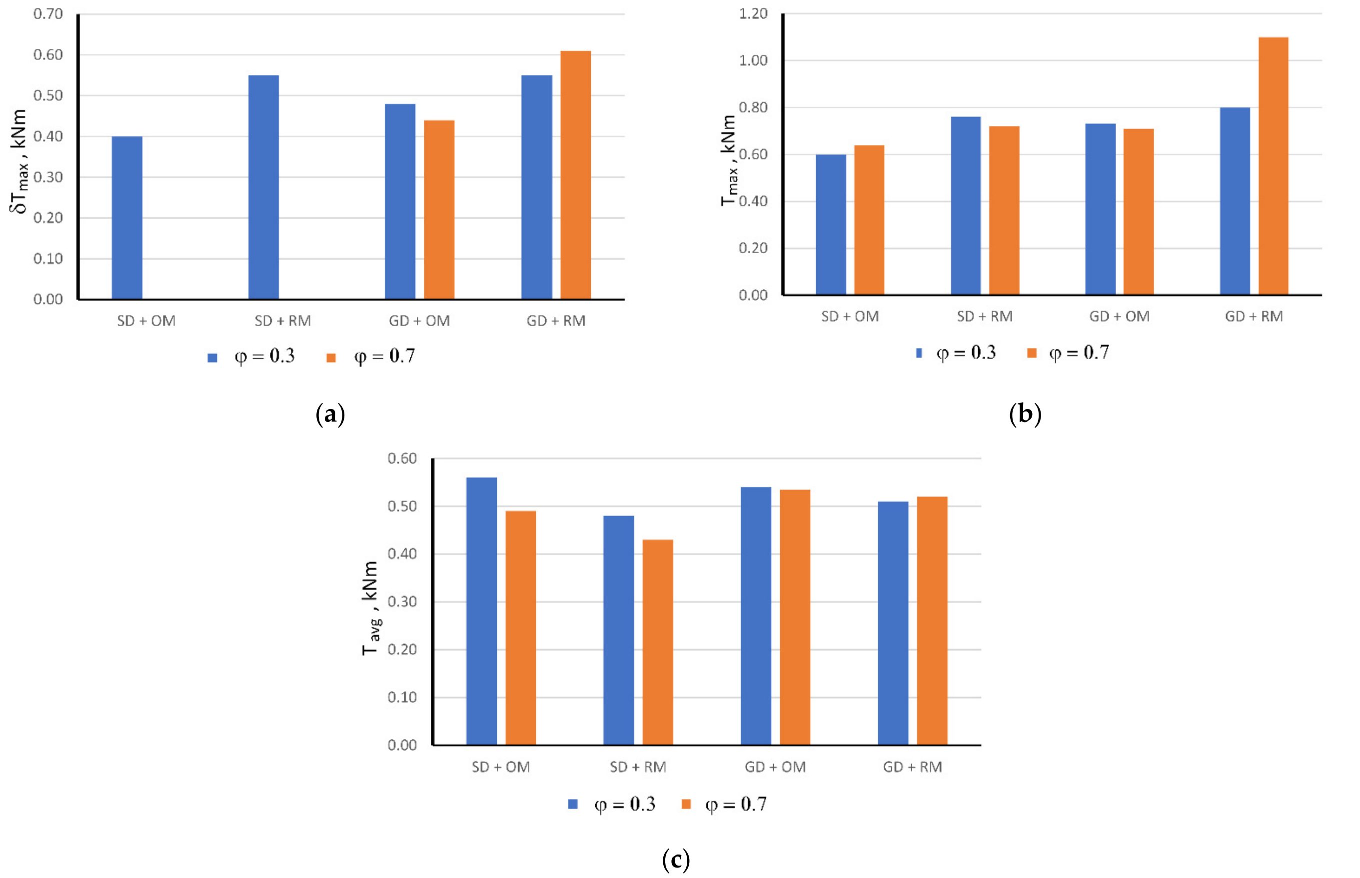

Figure 19. List of the values of the maximum differences in moments (**a**), maximum moments (**b**), and the values of the average moments (**c**) when the vehicle model was driven through the ditch at different maximum values of the coefficient of adhesion: GD—gear-type flow divider, SD—spool-type flow divider, OM—orbital motor, RM—radial piston motor.

4. Conclusions

The paper presents the results of research on the influence of the hydraulic drivetrain configuration on kinematic discrepancy and energy consumption during the overcoming of obstacles in a 6 × 6 all-wheel hydraulic drive vehicle.

The research showed a significant influence of the configuration of the drive system on the kinematic discrepancy (up to 195%) and energy consumption during off-road driving (about 15%). The greatest differences in the rotational speed of the wheels (about 200%) occurred in the systems in which the tested hydraulic motors were compiled in slide flow dividers. As a result, it should be recognized that systems with slide dividers are characterized by lower kinematic stiffness and, thus, a greater ability to compensate for the kinematic inconsistency (up to 79%). On the other hand, larger ones were found to be more energy-consuming. In systems using gear dividers, the value of moments generated on the wheels while overcoming obstacles was approximately 20–30% higher than in systems with slide dividers. In the drive systems in which the spool dividers were used, greater sensitivity of the change in the assessed parameters to the change in the value of the adhesion coefficient was also observed compared to the systems with gear dividers.

Due to the greater efficiency of systems with gear dividers, further research should be focused on examining the possibility of increasing their flexibility through the use of active digital flow control valves or the use of actively controlled external braking systems for each wheel separately. Particular attention should be paid to the efficiency of such a system, and the obtained results should be compared to the results obtained for the system with a spool divider. In addition, further works could be focused on the research of the possibility of negotiating other types of obstacles and driving on the ground with variable traction characteristics.

Author Contributions: Conceptualization, M.P.; methodology, M.P.; software, M.P.; validation, M.P.; formal analysis, A.R.; investigation, M.P.; resources, A.R.; data curation, K.C.; writing—original draft preparation, A.R. and M.P.; writing—review and editing, M.J.Ł.; visualization, P.K.; supervision, M.J.Ł.; project administration, M.M.; funding acquisition, A.R. All authors have read and agreed to the published version of the manuscript.

Funding: This research was funded by the Military University of Technology under project number UGB 22—757/2022, "Rozwój technik wytwarzania konstrukcji mechanicznych i systemów sterowania maszynami".

Institutional Review Board Statement: Not applicable.

Informed Consent Statement: Not applicable.

Data Availability Statement: Not applicable.

Conflicts of Interest: The authors declare no conflict of interest.

References

1. Andreev, A.F.; Kabanau, V.I.; Vantsevich, V.V. *Driveline Systems of Ground Vehicles: Theory and Design*; CRC Press: Boca Raton, FL, USA, 2010; ISBN 9781439817278.
2. Vukovic, M.; Leifeld, R.; Murrenhoff, H. Reducing Fuel Consumption in Hydraulic Excavators—A Comprehensive Analysis. *Energies* **2017**, *10*, 687. [CrossRef]
3. Janosevic, D.; Petrovic, G.; Petrovic, N. Hydrostatic transmissions calculation for mobile machines. In Proceedings of the 49th Anniversary of Faculty of Technical Schences, Machine Design, Novi Sad, Serbia, 18 May 2009; pp. 173–176.
4. Vorozhtsov, O.V.; Plaksin, I.E.; Trifanov, A.V. Application of gear hydraulic machines in the composition of hydrostatic transmissions. *IOP Conf. Series Earth Environ. Sci.* **2022**, *979*, 012023. [CrossRef]
5. Patrosz, P. Influence of Properties of Hydraulic Fluid on Pressure Peaks in Axial Piston Pumps' Chambers. *Energies* **2021**, *14*, 3764. [CrossRef]
6. Ito, Y.; Sarumaru, T. Analysis of Characteristic Performance of Hydrostatic Transmission for Vehicles. *Bull. JSME* **1976**, *19*, 1504–1514. [CrossRef]
7. Marelli, M.; Zarotti, L.G. Hydrostatic transmission with traction control. In Proceedings of the 22nd Internation Symposium on Automation and Robotics in Construction ISARC, Ferrara, Italy, 11–14 September 2005. [CrossRef]
8. Przybysz, M.; Rubiec, A. Identification research of wheels angular velocity synchronization accuracy for 6 × 6 hydrostatically driven mobile robot. Transport Means. In Proceedings of the 21st International Scientific Conference Transpor Means, Juodkrantė, Lithuania, 20–22 September 2017; pp. 204–212.
9. Dudziński, P.; Skurjat, A. Impact of Hydraulic System Stiffness on Its Energy Losses and Its Efficiency in Positioning Mechanical Systems. *Energies* **2022**, *15*, 294. [CrossRef]
10. Jaskółowski, M.; Krogul, P.; Łopatka, M.; Muszyński, T.; Przybysz, M. Simulation research on terrain mobility of wheeled UGV for dismounted operation support. Proceeding of the 13th European Conference of ISTVS, Rome, Italy, 21–23 October 2015; ISBN 9781942112471.
11. Dadhich, S.; Bodin, U.; Andersson, U. Key challenges in automation of earth-moving machines. *Autom. Constr.* **2016**, *68*, 212–222. [CrossRef]
12. Ahopelto, M. Towards Automation and Improved Fuel Economy with System Architecture Design of a Non-Road Working Machine. Ph.D. Thesis, Tampere University, Tampere, Finland, 2019.
13. Cieślik, K.; Krogul, P.; Rubiec, A.; Spadło, K. Concept of a vehicle for collecting and transporting baled biomass. In Proceedings of the 10th International Conference ITELMS 2015, Panevezys, Lithuania, 21–22 May 2015; pp. 69–74.
14. Przybysz, M.; Łopatka, M.; Małek, M.; Rubiec, A. Influence of Flow Divider on Overall Efficiency of a Hydrostatic Drivetrain of a Skid-Steer All-Wheel Drive Multiple-Axle Vehicle. *Energies* **2021**, *14*, 3560. [CrossRef]
15. Eckert, J.J.; Barbosa, T.P.; da Silva, S.F.; Silva, F.L.; Silva, L.C.; Dedini, F.G. Electric hydraulic hybrid vehicle powertrain design and optimization-based power distribution control to extend driving range and battery life cycle. *Energy Convers. Manag.* **2022**, *252*, 115094. [CrossRef]
16. Sokar, I.; Murrenhoff, H. Research on series hydraulic hybrid drivetrain for using in automobile. In Proceedings of the 14th ANME Conference, Vail, CO, USA, 17–20 October 2010.
17. Azzam, I.; Pate, K.; Garcia-Bravo, J.; Breidi, F. Energy Savings in Hydraulic Hybrid Transmissions through Digital Hydraulics Technology. *Energies* **2022**, *15*, 1348. [CrossRef]
18. Mulders, S.P.; Diepeveen, N.F.B.; van Wingerden, J.-W. Control design, implementation, and evaluation for an in-field 500 kW wind turbine with a fixed-displacement hydraulic drivetrain. *Wind Energy Sci.* **2018**, *3*, 615–638. [CrossRef]

19. Burgos, D.A.T.; Orozco, C.E.D. Fuzzy Control of velocity for a hydrostatic transmission. *Rev. Fac. Ing.* **2008**, *44*, 137–143.
20. Zavadinka, P.; Krissak, P. Simulation of vehicle working conditions with hydrostatic pump and motor control algorithm. *J. Autom. Mob. Robot. Intell. Syst.* **2012**, *6*, 40–46.
21. Cook, J.T.; Ray, L.E.; Lever, J.H. Mobility Enhancement of Heavy-Duty Tracked Vehicles Under Load Using Real-Time Terrain Characterization, Traction Control, and a Towing Winch. *J. Dyn. Syst. Meas. Control* **2019**, *141*, 071016. [CrossRef]
22. Bodin, A. Improving the Mobility Performance of Tracked Vehicles in Deep Snow. Ph.D. Thesis, Lulea University of Technology, Luleå, Sweden, 2002.
23. Belousov, A.M.; Karelin, D.L.; Boldyrev, A.V. Dynamic Analysis of Hydrostatic Transmission with an Axial Flow Divider. In *International Conference on Industrial Engineering (ICIE 2020)*; Springer: Cham, Switzerland, 2021. [CrossRef]
24. Vantsevich, V.; Augsburg, K.; Shyrokau, B.; Ivanov, V. Kinematic Discrepancy Minimization for AWD Terrain Vehicle Dynamics Control. *SAE Tech. Pap.* **2010**, *1*, 1895. [CrossRef]
25. Przybysz, M. Badania Niezgodności Kinematycznej Hydrostatycznych Układów Napędowych Bezzałogowych Platform Lądowych. Ph.D. Thesis, Military University of Technology, Warsaw, Poland, 2019.
26. Przybysz, M.; Rubiec, A. Simulation of kinematic discrepancy in multiaxis hydrostatic drive system. In Proceedings of the 11th International Conference on Intelligent Technologies in Logistics and Mechatronics Systems, Panevezys, Lithuania, 28–29 April 2016; pp. 131–140.
27. Bassani, R. Hydrostatic systems supplied through flow dividers. *Tribol. Int.* **2001**, *34*, 25–38. [CrossRef]
28. Vantsevich, V.V. Multi-wheel drive vehicle energy/fuel efficiency and traction performance: Objective function analysis. *J. Terramechanics* **2007**, *44*, 239–253. [CrossRef]
29. Comellas, M.; Pijuan, J.; Potau, X.; Noguès, M.; Roca, J. Efficiency sensitivity analysis of a hydrostatic transmission for an off-road multiple axle vehicle. *Int. J. Automot. Technol.* **2013**, *14*, 151–161. [CrossRef]
30. Wong, J.Y. *Theory of Ground Vehicles*; John and Wiley and Sons: Hoboken, NJ, USA, 2008; ISBN 978-0-470-17038-0.